UNIVERSITY of York

This is a repository copy of *Golden single-atomic-site platinum electrocatalysts*.

White Rose Research Online URL for this paper:
https://eprints.whiterose.ac.uk/134816/

Version: Accepted Version

---

**Article:**
Duchesne, Paul, Li, Z.Y., Deming, Christopher et al. (10 more authors) (2018) Golden single-atomic-site platinum electrocatalysts. Nature Materials. pp. 1033-1039. ISSN 1476-1122

https://doi.org/10.1038/s41563-018-0167-5

---

**Reuse**
Items deposited in White Rose Research Online are protected by copyright, with all rights reserved unless indicated otherwise. They may be downloaded and/or printed for private study, or other acts as permitted by national copyright laws. The publisher or other rights holders may allow further reproduction and re-use of the full text version. This is indicated by the licence information on the White Rose Research Online record for the item.

**Takedown**
If you consider content in White Rose Research Online to be in breach of UK law, please notify us by emailing eprints@whiterose.ac.uk including the URL of the record and the reason for the withdrawal request.

White Rose university consortium
Universities of Leeds, Sheffield & York

eprints@whiterose.ac.uk
https://eprints.whiterose.ac.uk/

# Golden Single-atomic-site Platinum Electrocatalysts

Paul N. Duchesne,[†] Z.Y. Li,[‡,#] Christopher P. Deming,[§,#] Victor Fung,[⊥,#] Xiaojing Zhao,[‖] Jun Yuan,[▽] Tom Regier,[O] Ali Aldalbahi,[¶] Zainab Almarhoon,[¶] Shaowei Chen,[§] De-en Jiang,[⊥] Nanfeng Zheng,[‖] and Peng Zhang*[,†]

[†] Department of Chemistry, Dalhousie University, 6274 Coburg Road, Halifax, NS, Canada

[‡] Nanoscale Physics Research Laboratory, School of Physics & Astronomy, University of Birmingham, Birmingham, B15 2TT, UK

[§] Department of Chemistry and Biochemistry, University of California, Santa Cruz, CA 95064, USA

[⊥] Department of Chemistry, University of California, Riverside, CA 92521, USA

[‖] State Key Laboratory for Physical Chemistry of Solid Surfaces, and Collaborative Innovation Center of Chemistry for Energy Materials, College of Chemistry and Chemical Engineering, Xiamen University, Xiamen 361005, China

[▽] Department of Physics, University of York, York, YO10 5DD, UK

[O] Canadian Light Source, Saskatoon, SK, Canada

[¶] Department of Chemistry, College of Science, King Saud University, P.O. Box 2455, Riyadh 11451, Kingdom of Saudi Arabia

[*] Corresponding author, Email: peng.zhang@dal.ca

[#] Equally contributing second authors

Keywords: gold, platinum, colloidal synthesis, single-atomic site, alloy bonding, electrocatalysis, formic acid oxidation

## Abstract

Bimetallic nanoparticles with tailored structure constitute a desirable model system for catalysts, as crucial factors such as geometric and electronic effects can be readily controlled by tailoring the structure and alloy bonding of the catalytic site. Herein, we report a facile colloidal method to prepare a series of platinum-gold (PtAu) nanoparticles with tailored surface structures and particle diameters on the order of 7 nm. Samples with low Pt content, particularly $Pt_4Au_{96}$, exhibited unprecedented electrocatalytic activity for the oxidation of formic acid. A high forward current density of 3.77 $A \cdot mg_{Pt}^{-1}$ was observed for $Pt_4Au_{96}$, a value two orders of magnitude greater than those observed for core-shell-structured $Pt_{78}Au_{22}$ and a commercial Pt nanocatalyst. Extensive structural characterization and theoretical DFT simulations of the best-performing catalysts revealed densely packed single-atom Pt surface sites surrounded by Au atoms, suggesting that their superior catalytic activity and selectivity could be attributed to the unique structural and alloy bonding properties of these single-atomic-site catalysts.

Platinum (Pt) has a long history of use in catalysis, due primarily to its high activity in a wide range of chemical reactions.[1] However, it faces major obstacles in some reactions, including the problem of carbon monoxide (CO) poisoning in the formic acid oxidation (FAO) reaction.[2] Due to the very strong binding affinity of CO at Pt surfaces, exposure to even small quantities of CO can gradually poison (*i.e.*, deactivate) a Pt catalyst.[3] In recent years, it has become common to alloy Pt with other metals in order to modify its catalytic properties;[4–7] thus, it seems reasonable this approach could also be used to address the issue of CO poisoning and enhance the performance of such Pt catalysts.[8,9] Recent advances in nanoparticle synthesis have allowed for the preparation of bimetallic nanocatalysts with increasingly well-defined alloy structures.[10–13] An important quality of these bimetallic nanoparticles is that the interaction between atoms of different metals at the nanoparticle surface can result in significantly enhanced catalytic activity due to both geometric and electronic effects.[14–16] By definition, these alloy interactions occur at the boundaries between domains of the two metals; thus, any catalytic enhancement effect should also be maximized by increasing the degree of intermetallic mixing at the nanoparticle surface.[16] A very interesting and little-researched limit to this mixing is found in single-Pt-site catalysis in an alloy nanoparticle system, wherein distinct geometric and electronic effects set it apart from other phase-segregated surface nanostructures via the so-called "ensemble effect" theory.[17–21]

Herein is presented a series of colloidal bimetallic PtAu nanoparticles, obtained via a facile solution-phase synthesis, that feature stable single-atomic Pt catalytic sites with high FAO activity. Electrocatalytic measurements reveal a remarkable enhancement in activity that is highly dependent on the PtAu composition of the sample. Characterization of such materials is very challenging, as Pt and Au have nearly identical atomic numbers. Nonetheless, we demonstrate that convincing conclusions can be achieved through the use of several complementary techniques, including X-ray absorption spectroscopy (XAS), X-ray photoelectron spectroscopy (XPS), energy dispersive X-ray spectroscopy (EDX), high-angle annular dark-field scanning transmission electron microscopy (HAADF-STEM), and electrochemical measurements, with each offering its own insights into the structure of the subject material. The results of this structural characterization, together with density functional theory (DFT) modeling, demonstrate that it is not only elemental composition that dictates the

electrocatalytic activity of the PtAu nanoparticles, but that the local bonding environment of single-atomic-site Pt surface atoms plays the most critical role.

The bimetallic PtAu nanoparticles used in this study were prepared from stock solutions of Pt and Au chloride precursor salts using a colloidal synthetic method adapted from that of Chen *et al.*[16] This synthetic procedure and a complete set of the PtAu samples with systematically varied compositions from 4% Pt to 96% Pt are provided in Supplementary Fig. 1. An illustration of nanoparticle formation from ions in solution is shown in Fig. 1a. Of particular importance was the replacement of the CO reducing agent/co-ligand (used in the original synthesis) with ethylene glycol (EG), such that the PtAu nanoparticles were prepared in a CO-free environment. Following synthesis, these nanoparticles were deposited onto a carbon powder support material in preparation for catalytic activity testing. Transmission electron microscopy (TEM) was employed to confirm successful sample preparation (see Supplementary Fig. 2), and inductively coupled plasma optical emission spectroscopy (ICP-OES) was used to measure relative elemental compositions and mass loadings (see Supplementary Table 1). TEM results confirmed a high degree of nanoparticle dispersion and uniformity, with observed mean particle diameters of *ca.* 7 nm for all samples, and ICP-OES measurements revealed an average mass loading of 11 ± 2 wt% for the carbon-supported samples. The measured elemental compositions from ICP-OES (*i.e.*, $Pt_{78}Au_{22}$, $Pt_{53}Au_{47}$, $Pt_{17}Au_{83}$, $Pt_7Au_{93}$, and $Pt_4Au_{96}$) corresponded closely to the nominal concentrations of Pt and Au used during synthesis, and are hereafter used to distinguish between PtAu samples.

CV analysis yielded a very interesting result regarding the specific electrocatalytic activities of the PtAu nanoparticles. As can be seen from the magnitude of the Pt-mass-normalized current peaks at *ca*. 0.6 $V_{RHE}$ in the anodic sweeps (see Fig. 1b), the highest activities were observed for those samples containing the least Pt. The most active sample, $Pt_4Au_{96}$, exhibited activity greater than that of the commercial Pt/C catalyst and least-active PtAu nanoparticle sample by up to two orders of magnitude (*i.e.*, 126 times greater than $Pt_{78}Au_{22}$, and 90 times greater than Pt/C). A strong correlation was observed between low FAO peak currents and the presence of a significant peak at *ca.* 0.85 $V_{RHE}$ in the CV plot. This secondary peak arises from the electrochemical oxidation of adsorbed CO molecules, which are well known to poison the surface of Pt and suppress its catalytic activity.[22] The absence of such a peak in the CV plots of those PtAu nanoparticles containing the least Pt suggests that resistance to CO poisoning may

play a significant role in their enhanced catalytic activity. It should be noted that characterization of pure Au nanoparticles, prepared according to the same protocol, revealed no measureable activity in the FAO reaction (see Supplementary Fig. 3).

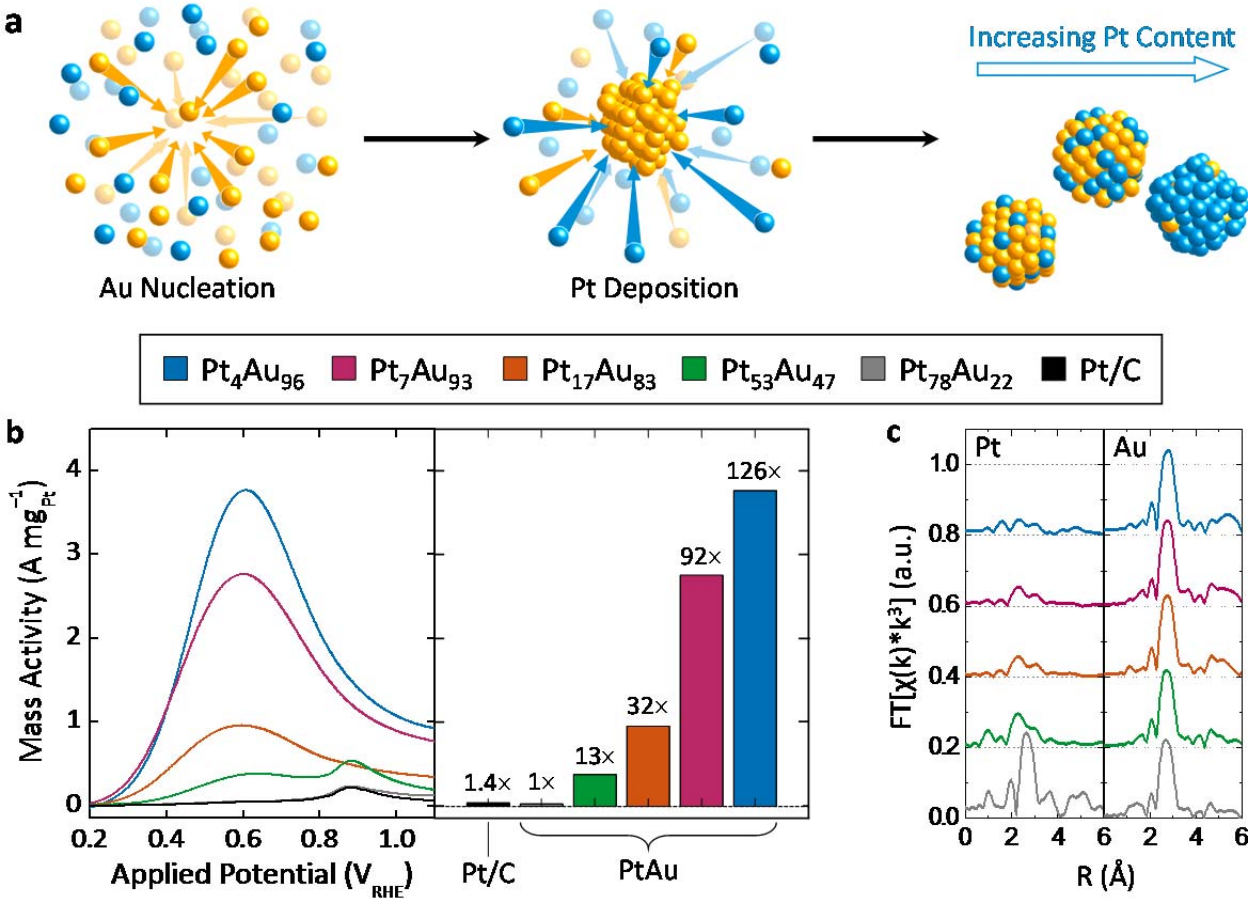


**Fig. 1 | Synthesis, reactivity and EXAFS of catalysts. a**, Illustration of nanoparticle formation via reduction of solvated ions. **b**, Pt mass-normalized anodic sweeps obtained from PtAu nanoparticle catalysts in electrolyte containing 0.1 M concentrations of both $HClO_4$ and HCOOH, with peak currents graphed for comparison. The data acquired from a commercial Pt/C catalyst is included to provide additional context. **c**, Plotted FT-EXAFS spectra obtained from Pt and Au $L_3$-edge absorption spectra of PtAu nanoparticles, illustrating the drastic under-coordination of Pt atoms in low-Pt-content samples such as $Pt_7Au_{93}$ and $Pt_4Au_{96}$.

In order to gain a structural perspective on this activity enhancement, FT-EXAFS analysis was performed on the PtAu nanoparticles at the Pt and Au $L_3$ absorption edges, shown in Fig. 1c. Detailed information regarding the local Pt and Au bonding environments in each sample was obtained by fitting these spectra (see Supplementary Fig. 4), resulting in the structural parameter values shown in Table 1. Observed trends in coordination number and bond length values are also presented graphically in Supplementary Fig. 5. While the scattering paths

involving Pt and Au atoms were too similar to produce separable peaks in the FT-EXAFS spectrum (see Supplementary Fig. 6 for a topographical illustration), this similarity made it possible to treat scattering from both Pt and Au as a single path (denoted Pt–M and Au–M for the Pt and Au $L_3$-edges, respectively). Analysis of the resulting bond lengths suggested that Pt atoms in $Pt_7Au_{93}$ and $Pt_4Au_{96}$, the most highly active PtAu samples, were present almost exclusively as single-atom sites surrounded by atoms of Au. This observation is based on the close agreement between the measured Pt–M bond lengths (2.82 Å) and the expected bimetallic bond length of 2.822 Å for a homogenous PtAu alloy, as calculated from experimental Pt–Pt and Au–Au bond lengths in pure Pt and Au nanoparticles (see Supplementary Table 2). Further evidence for the single-atom structure of Pt in these two samples is provided via HAADF-STEM, electrochemistry and XPS valence band analyses. It is notable that a similar Pt–M bond distance was also observed for $Pt_{17}Au_{83}$; however, its Pt–M coordination number (CN) is identical to that of the core-shell structured nanoparticles ($Pt_{53}Au_{47}$ and $Pt_{78}Au_{22}$) and considerably higher than the single-atom Pt samples. These results indicate that $Pt_{17}Au_{83}$ exhibits a mixed structure containing both single-atom and few-atom Pt cluster regions, with more of them located within the core of the nanoparticle. Additional support for this conclusion is provided by the particularly large Debye-Waller coefficient ($\sigma^2$) value obtained for $Pt_{17}Au_{83}$, indicating that there is greater variation among the Pt–M bond lengths due to significant contributions from both Pt–Pt and Pt–Au bonds. Further evidence will also be provided in the electrochemical and valence band studies.

**Table 1 | Structural parameter values for PtAu nanoparticles.**

| | Pt–M | | | | Au–M | | | |
|---|---|---|---|---|---|---|---|---|
| **Sample** | **CN** (atoms) | **R** (Å) | **$\sigma^2$** ($10^{-3}$ Å$^2$) | **$\Delta E_0$** (eV) | **CN** (atoms) | **R** (Å) | **$\sigma^2$** ($10^{-3}$ Å$^2$) | **$\Delta E_0$** (eV) |
| $Pt_{100}Au_0$ | 11.1(5) | 2.772(1) | 2.1(2) | 3.9(4) | ----- | ----- | ----- | ----- |
| $Pt_{78}Au_{22}$ | 9(1) | 2.776(4) | 2.6(6) | 3(1) | 12(1) | 2.839(4) | 4.3(6) | 0(1) |
| $Pt_{53}Au_{47}$ | 9(2) | 2.776(8) | 3(2) | 2(1) | 12.1(9) | 2.851(3) | 4.2(4) | 2.3(7) |
| $Pt_{17}Au_{83}$ | 9(1) | 2.818(5) | 8(1) | 2.8(8) | 11.6(9) | 2.861(3) | 3.6(4) | 2.6(7) |
| $Pt_7Au_{93}$ | 7.4(9) | 2.813(5) | 6(1) | 2.6(8) | 12(1) | 2.862(4) | 3.4(5) | 2(1) |
| $Pt_4Au_{96}$ | 5(2) | 2.82(2) | 4(3) | 3(3) | 11.0(8) | 2.871(2) | 3.1(3) | 3.4(6) |
| $Pt_0Au_{100}$ | ----- | ----- | ----- | ----- | 12.0(4) | 2.872(1) | 3.4(2) | 2.7(3) |

These parameter values were obtained by fitting the respective Pt and Au $L_3$-edge FT-EXAFS spectra of each nanoparticle sample. Numbers in parenthesis indicate the uncertainty (1σ) in the last digit of the corresponding value.

EXAFS analysis of local CNs revealed that Pt atoms were under-coordinated in the PtAu nanoparticles, especially those bearing highly active single-atom sites. CNs for the Pt–M scattering path ranged from 9 nearest neighbours in $Pt_{78}Au_{22}$ to just 5 in $Pt_4Au_{96}$, standing in stark contrast with the CN of 11 observed for pure Pt nanoparticles synthesized using the same method. Combined with Au–M CNs on the order of 11 to 12 nearest neighbours, this evidence strongly suggests an Au-core/PtAu shell nanoparticle structure, with Pt predominantly located at surface sites. Furthermore, Pt concentrations measured using surface-sensitive X-ray photoelectron spectroscopy (XPS) were consistently greater than those obtained using bulk-sensitive ICP-OES (see Supplementary Fig. 7), providing convincing evidence of Pt surface-enrichment in all PtAu nanoparticle samples. The very low CNs observed for $Pt_7Au_{93}$ and $Pt_4Au_{96}$ (7 and 5, respectively) further indicate that Pt should be predominantly found on the particle surface with high-level surface roughness, including edge and corner sites.[12] X-ray absorption near edge structure (XANES) analysis of samples (see Supplementary Fig. 8) further confirmed the metallic nature of both Pt and Au in these nanoparticles, and provided support for the presence of single-atom Pt sites via a positive binding energy shift and increased white line breadth (both indicative of increasingly isolated Pt atoms[23]). This high degree of direct Pt–Au interaction was also observed in the XPS data, which featured a negative shift of the Pt 4f electron binding energies of $Pt_{17}Au_{83}$ and $Pt_4Au_{96}$ (as was shown in Supplementary Fig. 7). In contrast to the extensive Pt–Au mixing in those samples with a low Pt content, $Pt_{53}Au_{47}$ and $Pt_{78}Au_{22}$ exhibited predominantly Pt–Pt bonding, reflecting their more complete Au-core/Pt-shell structures.

The emerging picture of these nanoparticles as containing Pt preferentially located at the surface of Au cores is consistent with real space imaging of these nanoparticles using atomic resolution high angle annular dark field scanning transmission electron microscopy (HAADF-STEM) and elemental imaging using spatially resolved energy dispersive X-ray (EDX) spectroscopy (see Fig. 2a-c). In order to prevent beam damage to these nanoparticles, electron beam intensity was minimized during EDX spectroscopy measurements, which resulted in low X-ray counting statistics; nonetheless, there is strong evidence for Au signal originating

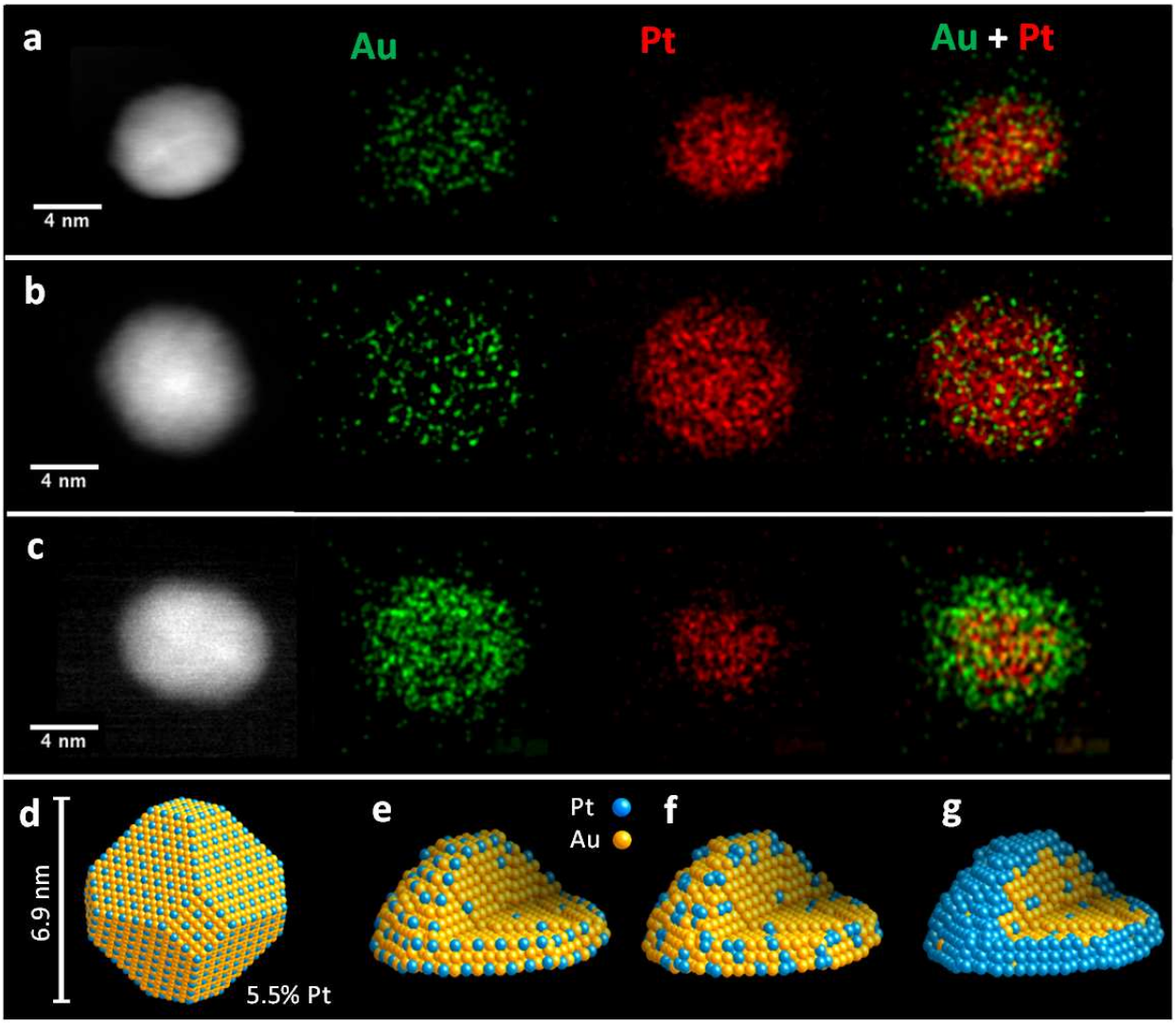


**Fig. 2 | HAADF-STEM images and structural models.** **a**, **b**, **c**, STEM/EDX mapping images of individual particles from $Pt_4Au_{96}$ and $Pt_7Au_{93}$ single-atom Pt, and $Pt_{78}Au_{22}$ core-shell samples, respectively. **d**, Structural model of an ideal, truncated octahedral nanoparticle with optimal single-atomic site coverage. Though strictly not representative of the nanoparticles synthesized herein, this model provides a reasonable estimate of the upper concentration limit for such single-atom Pt sites. **e**, **f**, **g**, Models depicting the proposed evolution of PtAu surface structures from single-atom Pt sites to few-atom Pt clusters to a complete Pt shell, respectively, as a result of increased Pt content.

mainly from the cores of nanoparticles, with the Pt signal being more diffuse and slightly enhanced at the particle edges. This effect can also be illustrated by comparing the overlay EDX maps of representative particles shown in Fig.2a-c. It is noteworthy that similar control over surface structure generally requires two or more sequential steps during synthesis, as Pt and Au are capable of forming homogeneous alloys.[23–26] The ability to achieve these complex surface

morphologies in a single reaction step likely stems from a combination of factors, including sequential reduction (due to the more negative reduction potential of Au relative to Pt) and preferential coordination of stabilizing amine ligands to surface Pt sites rather than Au sites.[27,28] The significantly greater adsorption energy of the oleylamine ligand molecules at surface Pt sites can contribute to the preferential Au-core/Pt-shell structure of the PtAu nanoparticles, as it results in greater stabilization and limits further deposition of Au atoms, thereby resulting in a Pt-enriched surface.

The observation of a Pt-rich surface is consistent with a single-atom Pt surface structure. For an ideal truncated octahedral nanoparticle (see Fig. 2d), maximum surface coverage by single-atomic sites (*i.e.*, with no co-adjacent Pt atoms) is achieved with a Pt content of 5.5%. While atomic-scale HAADF-STEM images suggest that the PtAu nanoparticles synthesized herein are predominantly polycrystalline, this single-crystalline estimate serves as a reasonable upper concentration limit at which exclusively single-atom Pt sites are able to exist, and suggests that $Pt_4Au_{96}$ and $Pt_7Au_{93}$ could reasonably exhibit such a surface morphology.

Based on the available information, the PtAu samples can now be categorized in terms of their surface structure: Au with single-atom Pt sites ($Pt_7Au_{93}$ and $Pt_4Au_{96}$), Au with single-atom and few-atom Pt sites ($Pt_{17}Au_{83}$), and Au-core/Pt-shell ($Pt_{78}Au_{22}$ and $Pt_{53}Au_{47}$). This gradual change from single-atomic to near-complete shell coverage in these PtAu/C nanocatalysts is illustrated in Fig. 2e-g. Additional support for the proposed surface structures of the nanoparticles can be found in the detailed analysis of their electrocatalytic performance presented in Fig. 3. The disappearing peak at *ca.* 0.85 $V_{RHE}$ in Fig. 1b is more clearly shown in the first-derivative plots of Pt mass activity in Fig. 3a. Such peak intensity was completely absent in both the $Pt_7Au_{93}$ and $Pt_4Au_{96}$ samples (as is more clearly illustrated in Supplementary Fig. 9), and was markedly reduced in $Pt_{17}Au_{83}$. These electrochemical results offer another piece of evidence for the Pt single-atom structure in $Pt_7Au_{93}$ and $Pt_4Au_{96}$. As is illustrated in Fig. 3c, the existence of adjacent Pt surface sites will produce a CO poisoning peak in the first derivative voltammogram, whereas the single-atom Pt geometry of the catalyst surface will encourage the $CO_2$ formation via the dehydrogenation mechanism. Moreover, the small CO first derivative peak for $Pt_{17}Au_{83}$ in Fig. 3a illustrates the existence of some smaller, cluster-like Pt domains in this sample. Fig. 3b shows that a similar trend in specific activity is observed when normalizing FAO anodic sweep voltammograms by the electrochemically active surface area (ECSA) of Pt,

indicating again that the observed increase in activity was not simply due to an increased proportion of Pt surface sites in those samples with lower Pt content. Both $Pt_7Au_{93}$ and $Pt_4Au_{96}$ exhibited very similar peak intensities when the anodic sweeps were normalized by the combined ECSAs of Pt and Au, suggesting that they shared a similar surface structure in addition to their mutual resistance to CO poisoning. Finally, normalization of electrocatalytic performance by total metal catalyst mass resulted in a trade-off between reduced surface poisoning by CO and the number of available Pt catalytic sites (see Supplementary Fig. 10).

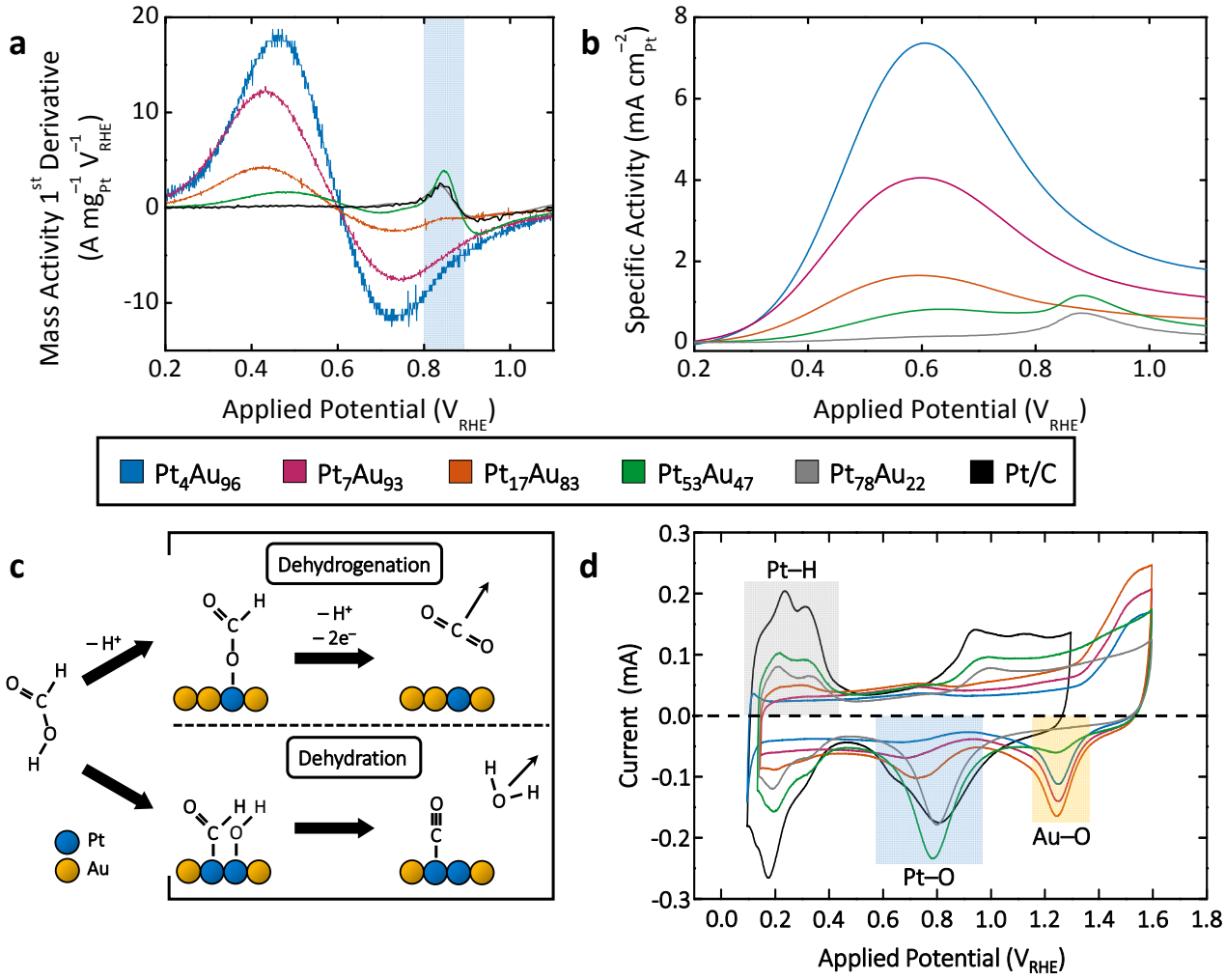


**Fig. 3 | Further electrochemical analysis. a**, First-derivative of Pt mass-normalized FAO voltammograms presented in Fig. 1a. The blue box highlights the sensitivity of the first-derivative peak at *ca.* 0.85 $V_{RHE}$ to the Pt surface structure. **b**, FAO anodic sweep voltammograms obtained from PtAu nanoparticle and commercial Pt/C catalyst samples, as normalized by the electrochemically active surface area of Pt. These voltammograms were also obtained using a sweep rate of 10 mV·s$^{-1}$ and an electrolyte containing 0.1 M concentrations of both $HClO_4$ and HCOOH. **c**, Schematic illustration of the dehydrogenation and dehydration mechanisms of FAO reactions on PtAu surfaces. **d**, Cyclic voltammograms from PtAu nanocatalysts (shown at full amplitude) and commercial Pt nanocatalysts (shown at half amplitude to facilitate comparison) acquired in 0.1 M $HClO_4$ with a sweep rate of 100 mV·s$^{-1}$.

This structure is experimentally supported by the behaviour of distinct Au–O adlayer formation on the exposed Au surfaces, as revealed by CV measurements under non-catalytic conditions (see Fig. 3d). Regions of interest include the positive Pt–H desorption peaks highlighted from *ca.* 0.1 to 0.4 $V_{RHE}$, and the negative Pt–O and Au–O adlayer removal peaks highlighted from 0.55 to 0.95 $V_{RHE}$ and from 1.15 to 1.35 $V_{RHE}$, respectively. As expected from the relative compositions, the areas of the Pt–O and Au–O adlayer removal peaks revealed a gradual transition from a pure Pt surface in $Pt_{78}Au_{22}$ (indicative of its Au-core/Pt-shell structure) to the predominantly Au surface decorated with Pt in $Pt_4Au_{96}$. In addition to a steady reduction of Pt–H peak area, a significant negative shift of the Pt–O adlayer removal peak was observed with decreasing Pt content; this shift reached a maximum of *ca.* 0.1 $V_{RHE}$ in $Pt_4Au_{96}$, revealing markedly strengthened Pt–O adsorption, likely due to the increasingly lowered coordination numbers of Pt atoms in these samples. This observation provides strong evidence for the thorough mixing of Pt and Au at the surface of samples with low Pt content, resulting in a relatively even distribution of Pt across the predominantly Au surface. The less-drastic shift of the Au–O adlayer desorption peak relative to that of Pt–O can be explained by the fact that any charge transfer effects involve up to 9 Au atoms per Pt atom, depending on the relative composition of the sample.

Given that CO poisoning has a drastic impact on the measured activity of Pt-based FAO catalysts, DFT calculations were performed to study the adsorption properties of CO at single-atom, few-atom, and pure Pt surfaces (see Fig. 4a-c). The (111) surface is selected in our DFT calculations since the (111) sites are the most abundant surface sites in regular colloidal Au and Pt nanoparticles. Multiple adsorption sites for CO exist at pure and few-atom Pt surfaces (in order of increasing adsorption energy: apical, bridging, hcp hollow, and fcc hollow), whereas only a single site (apical) was found to be significant for the single-atom Pt surface. The results of these calculations indicate that CO adsorption is weakened at all adsorption sites on both few-atom and single-atom Pt surfaces relative to bulk Pt (see Fig. 4d and Supplementary Table 3). Adsorption energies of CO at apical sites, for example, are reduced from –1.268 eV on bulk Pt to –1.063 and –1.032 eV on few-atom and single-atom surfaces, respectively. This finding is in line with the observed enhancement in FAO activity, rationalized via a weakening of the typically too-strong CO adsorption on Pt (as per the Sabatier Principal).[29,30] While this weakened CO

adsorption is consistent with the observed activity enhancement, however, it is generally recognized that the availability of adjacent adsorption sites also makes a significant contribution to FAO activity.[7] It is worthwhile to note that the PtAu nanoparticles also show significant retention of activity as shown by both chronoamperometric measurements performed at 0.55 $V_{RHE}$ and repeated cycling between 0.1 and 1.1 $V_{RHE}$ (Supplementary Fig. 11). These results further indicate the fairly good stability of the alloy-based single-atom catalysts, with the latter demonstrating that high activity (> 70% of the initial value) can be retained even after 1,500 successive rounds of potential cycling.

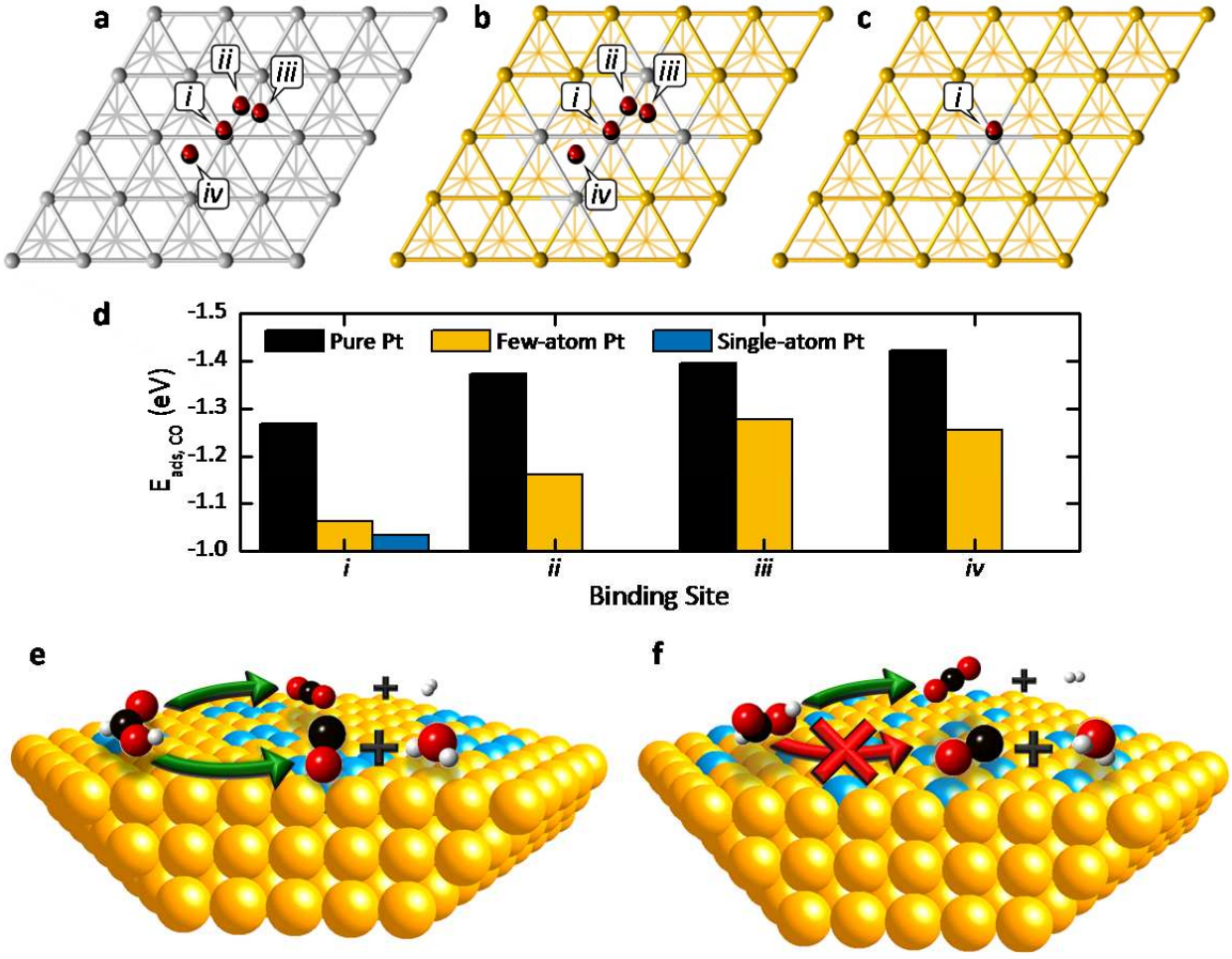


**Fig. 4 | DFT-calculated binding of CO at PtAu surfaces. a**, **b**, **c**, Illustration of CO adsorption modes on model (111) lattices of pure, few-atom, and single-atomic Pt surfaces, respectively, including apical (*i*), bridging (*ii*), hcp hollow (*iii*), and fcc hollow (*iv*) coordination sites. **d**, Calculated adsorption energies for the indicated CO adsorption sites. **e**, **f**, Predominant FAO reaction pathways on few-atom (or greater) and single-atom Pt surfaces, highlighting the selectivity achieved via the ensemble effect.

While a number of possible pathways exist for the oxidation of formic acid at Pt surfaces, the dehydrogenation and dehydration pathways tend to predominate, overall (see Fig. 4e).[30] The former pathway is responsible for the majority of the observed FAO activity of Pt, the latter is a major concern, as it leads to the formation of adsorbed CO species at Pt sites and blocks them from participating in future reaction steps. Due to its large impact on catalytic activity, surface morphology also plays a large role in determining which of these two reaction pathways will predominate. Both DFT calculations[31] and experimental evidence[32] support this observation, indicating that only one Pt adsorption site is required for formic acid dehydrogenation, whereas the indirect dehydration pathway requires a greater number of adjacent atoms. This so-called "ensemble effect" strongly discourages the detrimental indirect reaction, leaving the direct dehydrogenation reaction as the primary reaction pathway (see Fig. **Error! Reference source not found.**4f). Thus, the formation of isolated single-atom catalytic sites can be linked to the remarkable activity increases observed in these PtAu nanocatalysts.

Valence band analysis was also performed on the PtAu/C nanocatalyst using both DFT density of states (DOS) calculations and XPS measurements to better understand the electronic effect of alloy formation on catalytic activity. The DFT DOS results in Fig. 5a predict a drastic reduction of intensity near the Fermi level (*i.e.*, 0 eV) for the single-atomic PtAu surface relative to the pure Pt surface. Tellingly, in the XPS valence band measurements shown in Fig. 5b-e, the near-Fermi level DOS (*i.e.*, –2 to 0 eV) is also found to be very sensitive to the local structural environment of Pt. The two samples bearing single-atom Pt sites, $Pt_4Au_{96}$ and $Pt_7Au_{93}$, show the lowest DOS intensity in the near-Fermi level region, being virtually identical to the pure Au surface. In contrast, a pronounced increase in DOS intensity near the Fermi level is observed for the few-atom-cluster Pt sample, $Pt_{17}Au_{83}$. Finally, when a more complete Pt shell is formed at the Au nanoparticle surface in $Pt_{53}Au_{47}$, the near-Fermi level DOS becomes higher still and its intensity begins to approach that of the pure Pt surface.

The aforementioned results indicate that samples containing larger amounts of Pt demonstrate much more pronounced Pt character in their valence bands, resulting in increased DOS intensities near the Fermi level. For single-atom Pt surfaces, however, no such Pt–Pt bonding exists and the overall DOS is determined by the predominant Au–Au bonding. Thus, the low DOS intensities observed near the Fermi level of single-atom Pt surfaces arises from the large number of Au atoms relative to Pt. When Pt–Pt bonds begin to appear, as occurs in the few-

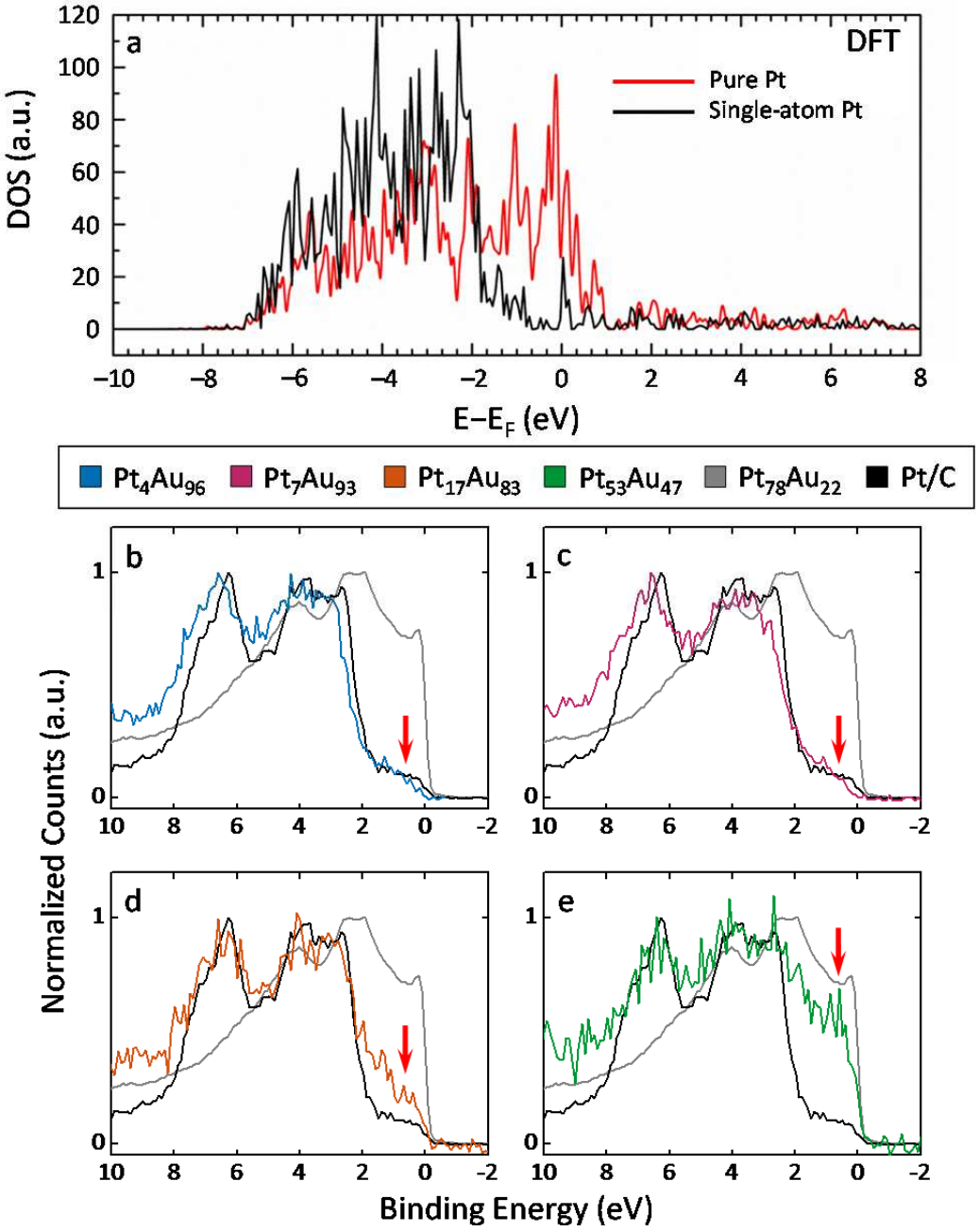


**Fig. 5 | Calculated and experimental DOS. a**, Calculated DFT density of states (DOS) plots corresponding to the pure and single-atom Pt surfaces used to calculate CO adsorption energies in Fig. 4a-d. **b**, **c**, **d**, **e**, XPS valence band spectra of $Pt_4Au_{96}$, $Pt_7Au_{93}$, $Pt_{17}Au_{83}$, and, $Pt_{53}Au_{47}$ samples compared against those of Pt and Au foil references. Red arrows indicate the near-Fermi level region, wherein samples containing single-atom Pt sites show considerable difference from those containing few-atom cluster and core-shell Pt surfaces.

atom Pt clusters of $Pt_{17}Au_{83}$, the DOS intensity of the near-Fermi level increases considerably. These results are in good agreement with previous observations that DOS intensity near the Fermi level is determined primarily by chemical bonding between like nearest neighbor atoms.[33] This means that the identical near-Fermi level DOS intensities observed for $Pt_4Au_{96}$, $Pt_7Au_{93}$, and the bulk Au reference prove, again, the single-atomic Pt structure for these two PtAu nanoparticle samples. Furthermore, the valence band structure of PtAu nanoparticle samples is also closely linked to their catalytic performance. Due to relativistic effects, the d-orbitals of Au are higher in energy, and the valence s-orbital lower, than would typically be expected, resulting in a shift of electron density from the former to the latter. As a result, Au atoms are less able to accept σ-donated electrons and engage in π back-donation to adsorbed CO molecules, weakening CO adsorption energies on these surfaces as was shown previously in Fig. 4.

In conclusion, bimetallic PtAu nanoparticles with extraordinary electrocatalytic FAO activity have been synthesized using a facile and easily tuneable colloidal method. By employing a comprehensive suite of structural characterization techniques, these PtAu nanocatalysts were identified as having distinct Au-core/Pt-shell, few-atom Pt cluster, or single-atom Pt surface structures, dictated by their relative elemental compositions. Structural characterization revealed a high surface density of low-coordinate, single-atom Pt sites in $Pt_7Au_{93}$ and $Pt_4Au_{96}$, which, according to the ensemble effect theory, prevented these catalysts from self-poisoning via CO generation at their surfaces. Thus, the observed orders-of-magnitude increase in Pt mass-normalized FAO activity for the best-performing PtAu nanocatalyst (single-atomic $Pt_4Au_{96}$) relative to the poorest (core-shell $Pt_{78}Au_{22}$ and commercial Pt) is readily explained in terms of surface structure and alloy bonding. DFT calculations further supported these results by revealing weakened adsorption of CO to few-atom and single-atom Pt surfaces as a result of both electronic effects arising from Pt-Au bonding interactions and the formation of discrete single-atom Pt catalytic sites (*i.e.*, the ensemble effect). Unlike many other published syntheses, only a single-step colloidal method was required to achieve a high degree of control over surface structure and alloy bonding, and a very high surface packing density of single-atom catalytic sites up to 7% can be achieved. As a result, the excellent electrocatalytic activity of these PtAu nanoparticles represents remarkable progress in the development of single-atomic-

site Pt catalysis, with their exceptional selectivity enabling the use of highly active Pt to perform reactions typically prohibited by CO poisoning.

## Methods

Methods, including statements of data availability and any associated accession codes and references, are available at https://doi.org/10.1038

## References


1. Chen, A. & Holt-Hindle, P. Platinum-based nanostructured materials: Synthesis, properties, and applications. *Chem. Rev.* **110,** 3767–3804 (2010).

2. Hunt, S. T. *et al.* Self-assembly of noble metal monolayers on transition metal carbide nanoparticle catalysts. *Science* **352,** 974–978 (2016).

3. Yu, Y., Wang, X. & Lim, K. H. A DFT study on the adsorption of formic acid and its oxidized intermediates on (100) facets of Pt, Au, monolayer and decorated Pt@Au surfaces. *Catal. Letters* **141,** 1872–1882 (2011).

4. Wang, X., He, B., Hu, Z., Zeng, Z. & Han, S. Current advances in precious metal core–shell catalyst design. *Sci. Technol. Adv. Mater.* **15,** 043502 (2014).

5. Liu, X., Wang, D. & Li, Y. Synthesis and catalytic properties of bimetallic nanomaterials with various architectures. *Nano Today* **7,** 448–466 (2012).

6. Liu, X., Wang, D. & Li, Y. Bimetallic nanocrystals: Liquid-phase synthesis and catalytic applications. *Adv. Mater.* **23,** 1044–1060 (2011).

7. Jiang, K., Zhang, H.-X., Zou, S. & Cai, W.-B. Electrocatalysis of formic acid on palladium and platinum surfaces : from fundamental mechanisms to fuel cell applications. *Phys. Chem. Chem. Phys.* **16,** 20360–20376 (2014).

8. Liu, J. *et al.* Tackling CO poisoning with single atom alloy catalysts. *J. Am. Chem. Soc.* **138,** 6396–6399 (2016).

9. Yuge, K., Koyama, Y., Kuwabara, A. & Tanaka, I. Surface design of alloy protection against CO-poisoning from first principles. *J. Phys. Condens. Matter* **26,** 355006 (2014).

10. Habrioux, A. *et al.* Structural and electrochemical studies of Au-Pt nanoalloys. *Phys. Chem. Chem. Phys.* **11,** 3573–3579 (2009).

11. Ji, X. *et al.* Nanocrystalline intermetallics on mesoporous carbon for direct formic acid fuel cell anodes. *Nat. Chem.* **2,** 286–293 (2010).

12. Zhang, H., Watanabe, T., Okumura, M., Haruta, M. & Toshima, N. Catalytically highly active top gold atom on palladium nanocluster. *Nat. Mater.* **11,** 49–52 (2012).

13. Guo, S. *et al.* Nanocatalyst superior to Pt for oxygen reduction reactions: The case of

core/shell Ag(Au)/CuPd nanoparticles. *J. Am. Chem. Soc.* **136,** 15026–15033 (2014).

14. Yang, X.-F. *et al.* Single-atom catalysts: A new frontier in heterogeneous catalysis. *Acc. Chem. Res.* **46,** 1740–1748 (2013).

15. Qiao, B. *et al.* Single-atom catalysis of CO oxidation using $Pt_1$/FeOx. *Nat. Chem.* **3,** 634–641 (2011).

16. Chen, G. *et al.* Interfacial effects in iron-nickel hydroxide-platinum nanoparticles enhance catalytic oxidation. *Science* **344,** 495–499 (2014).

17. Roy, A. *et al.* Enhanced catalytic activity of Ag/Rh bimetallic nanomaterial: Evidence of an ensemble effect. *J. Phys. Chem. C* **120,** 5457–5467 (2016).

18. Prinz, J. *et al.* Ensemble effect evidenced by CO adsorption on the 3-fold PdGa surfaces. *J. Phys. Chem. C* **118,** 12260–12265 (2014).

19. Zaera, F., Gellman, J. A. & Somorjai, G. A. Surface science studies of catalysis: Classification of reactions. *Acc. Chem. Res.* **19,** 24–31 (1986).

20. Ruff, M., Takehiro, N., Liu, P., Nørskov, J. K. & Behm, R. J. Size-specific chemistry on bimetallic surfaces: A combined experimental and theoretical study. *ChemPhysChem* **8,** 2068–2071 (2007).

21. Sachtler, W. M. H. Chemisorption complexes on alloy surfaces. *Catal. Rev. - Sci. Eng.* **14,** 193–210 (1976).

22. Stevanović, S. *et al.* Insight into the effect of Sn on CO and formic acid oxidation at PtSn catalysts. *J. Phys. Chem. C* **118,** 278–289 (2014).

23. Duchesne, P. N. & Zhang, P. Element-specific analysis of the growth mechanism, local structure, and electronic properties of Pt clusters formed on Ag nanoparticle surfaces. *J. Phys. Chem. C* **118,** 21714–21721 (2014).

24. Yu, Y., Hu, Y., Liu, X., Deng, W. & Wang, X. The study of Pt@Au electrocatalyst based on Cu underpotential deposition and Pt redox replacement. *Electrochim. Acta* **54,** 3092–3097 (2009).

25. Kim, J., Jung, C., Rhee, C. K. & Lim, T. Electrocatalytic oxidation of formic acid and methanol on Pt deposits on Au (111). *Langmuir* **23,** 10831–10836 (2007).

26. Luo, J. *et al.* Phase properties of carbon-supported gold-platinum nanoparticles with different bimetallic compositions. *Chem. Mater.* **17,** 3086–3091 (2005).

27. Atkins, P. & de Paula, J. in *Physical Chemistry* 1005–1006 (W.H. Freeman and Company, 2006).

28. Wu, B. & Zheng, N. Surface and interface control of noble metal nanocrystals for catalytic and electrocatalytic applications. *Nano Today* **8,** 168–197 (2013).

29. Bligaard, T. *et al.* The Brønsted–Evans–Polanyi relation and the volcano curve in heterogeneous catalysis. *J. Catal.* **224,** 206–217 (2004).

30. Zhong, W. & Zhang, D. New insight into the CO formation mechanism during formic acid oxidation on Pt(111). *Catal. Commun.* **29,** 82–86 (2012).

31. Neurock, M., Janik, M. & Wieckowski, A. A first principles comparison of the

mechanism and site requirements for the electrocatalytic oxidation of methanol and formic acid over Pt. *Faraday Discuss.* **140,** 363–378 (2009).

32. Cuesta, A., Escudero, M., Lanova, B. & Baltruschat, H. Cyclic voltammetry, FTIRS, and DEMS study of the electrooxidation of carbon monoxide, formic acid, and methanol on cyanide-modified Pt (111) electrodes. *Langmuir* **25,** 6500–6507 (2009).

33. Mason, M. Electronic structure of supported small metal clusters. *Phys. Rev. B* **27,** 748–762 (1983).

34. Schneider, C. A., Rasband, W. S. & Eliceiri, K. W. NIH Image to ImageJ: 25 years of image analysis. *Nat. Methods* **9,** 671–675 (2012).

35. Kraft, S., Stümpel, J., Becker, P. & Kuetgens, U. High resolution X-ray absorption spectroscopy with absolute energy calibration for the determination of absorption edge energies. *Rev. Sci. Instrum.* **67,** 681–687 (1996).

36. Bearden, J. A. X-ray wavelengths. *Rev. Mod. Phys.* **39,** 78–124 (1967).

37. Ressler, T. WinXAS: A program for X-ray absorption spectroscopy data analysis under MS-Windows. *J. Synchrotron Radiat.* **5,** 118–122 (1998).

38. Ankudinov, A. L., Ravel, B., Rehr, J. J. & Conradson, S. D. Real-space multiple-scattering calculation and interpretation of X-ray-absorption near-edge structure. *Phys. Rev. B* **58,** 7565–7576 (1998).

39. Wagner, C. D. in *Practical Surface Analysis* (eds. Briggs, D. & Seah, M. P.) 635–638 (1990).

40. Naumkin, A. V., Kraut-Vass, A., Gaarenstroom, S. W. & Powell, C. J. NIST X-ray photoelectron spectroscopy database. (2012). at <http://srdata.nist.gov/xps/>

41. Luo, S., Zhao, Y. & Truhlar, D. G. Improved CO adsorption energies, site preferences, and surface formation energies from a meta-generalized gradient approximation exchange–correlation functional, M06-L. *J. Phys. Chem. Lett.* **3,** 2975–2979 (2012).

## Acknowledgements

P.Z. acknowledges the financial support from the NSERC Canada Discovery Grant and P.N.D. was funded by an NSERC CGS scholarship. Financial supports from European COST Action MP0903 “Nanoalloy” (Z.Y.L.), and the U.S. National Science Foundation DMR-1409396 (S.C) are greatly acknowledged. Part of this work was supported by a PCOSS Open Project Grant (Xiamen University) awarded to P.Z. and hosted by N.Z. This research used resources of the Advanced Photon Source, an Office of Science User Facility operated for the U.S. Department of Energy (DOE) Office of Science by Argonne National Laboratory, and was supported by the U.S. DOE under Contract No. DE-AC02-06CH11357, and the Canadian Light Source and its

457 funding partners. The Canadian Light Source is supported by the CFI, NSERC, NRC, CIHR, the
458 University of Saskatchewan, the Government of Saskatchewan, Western Economic
459 Diversification Canada. We are also grateful for the assistance of Dr. Lari Leonardo for the
460 collection of additional EDX mapping in the JEOL-York Nanocenter using JEM-2200FS Cs-
461 corrected (S)TEM operating at 200kEV.

462

## 463 Author contributions

464 P.N.D synthesized all samples, conducted the XAS experiments and analysis, performed some of
465 the electrochemical and TEM studies, and wrote the manuscript. P.Z. designed the project,
466 coordinated the whole process of the work, and supervised P.N.D. to conduct this research.
467 Z.Y.L. and J.Y. performed the HAADF-STEM measurements and image analysis. C.P.D.
468 performed the electrochemical experiments under the supervision of S.C. V.F. conducted the
469 DFT calculations under the supervision of D.J. X.Z contributed to the TEM measurements under
470 the supervision of N.Z. A.A. and Z.A. also contributed to part of the TEM measurements. T.R.
471 performed some of the XPS measurements at the Canadian Light Source.

472

## 473 Competing Financial Interests

474 The authors declare no competing financial interests.

475

## 476 Additional information

477 Supplementary information is available for this paper at https://doi.org/10.1038

478

## 479 Methods

480 **Materials.** Dihydrogen hexachloroplatinate ($H_2PtCl_6 \cdot 6H_2O$, 99.9 %), hydrogen tetrachloroaurate
481 ($HAuCl_4 \cdot 3H_2O$, 99.9 %), ethylene glycol (EG, 99+ %), and HiSPEC 3000 carbon-supported Pt
482 catalyst (Pt/C, ≤ 500 ppm impurities) were purchased from Alfa Aesar. Oleylamine (OAm, C18-
483 content 80-90 %) and formic acid (HCOOH, 99 %) were purchased from Acros Organics.
484 Vulcan XC-72 carbon powder was purchased from Cabot. Nafion® 117 Solution (Nafion, 5 %)
485 and *n*-butylamine ($BuNH_2$, 99.5 %) were purchased from Sigma Aldrich. Perchloric acid
486 ($HClO_4$, 70 %) was purchased from Fisher Scientific. Ethanol used in cyclic voltammetry

experiments (EtOH, 96 %) was purchased from J.T. Baker. All reagents and solvents were used as received, without further purification.

**Synthesis of PtAu Nanoparticles.** PtAu nanoparticles were prepared from stock solutions of Pt and Au chloride precursor salts, with nominal compositions of 10, 25, 50, and 75 atom% Pt being selected by controlling the ratio of precursors used. In a typical synthesis, 72.5 mg $H_2PtCl_6 \cdot 6H_2O$ and 55.1 mg $HAuCl_4 \cdot 3H_2O$ were each dissolved in 70 mL of OAm through a combination of ultrasonication and manual mixing to obtain metal precursor stock solutions. Appropriate volumes of these Pt and Au stock solutions (prepared in OAm) were then added to a 100 mL round-bottom flask to give the desired Pt-to-Au ratio with a total volume of 20 mL. An additional 20 mL of EG was then added while mixing vigorously using a magnetic stirrer. The resulting mixture was subsequently bubbled with $N_{2(g)}$ for several minutes in order to remove dissolved $O_{2(g)}$ from solution. Each mixture was then placed in a 180 ºC oil bath, sealed, and allowed to react for 1 h. Once the reaction was complete, flask was removed from heat and allowed to cool to room temperature while still sealed under a $N_{2(g)}$ atmosphere. Due to the large excess of reducing agents employed in this reaction (OAm and EG, also functioning as solvents), all $Pt^{4+}$ and $Au^{3+}$ species can reasonably be assumed to have been reduced to a zero-valent state. In order to purify the product nanoparticles, each sample was divided amongst several 30 mL polypropylene centrifuge tubes. The nanoparticles were precipitated via addition of two to three volume equivalents of EtOH, and then isolated by centrifuging the resulting suspension (at 6,000 RPM for 5 min) and decanting the supernatant. The precipitated nanoparticles were then redispersed in hexanes via brief ultrasonication and shaking before being again precipitated and centrifuged. After this second centrifugation cycle, the purified nanoparticles were redispersed in hexanes and centrifuged once more to remove any insoluble material.

**Deposition of PtAu Nanoparticles onto XC-72 Carbon Powder.** Following purification, the nanoparticle samples were deposited onto an XC-72 carbon powder support material via ligand exchange-induced destabilization. A nanoparticle loading of 20 wt% (by total mass of Pt and Au) was selected in order to allow for better comparison with the commercial Pt/C catalyst (HiSPEC 3000, 20 wt% Pt) used as a reference material for electrocatalytic testing. For each sample, four mass equivalents of XC-72 powder (assuming a theoretical yield of 100 % for each nanoparticle sample) were added to 15 mL of $BuNH_2$ and thoroughly dispersed via ultrasonication. Each purified nanoparticle sample was then precipitated using EtOH and isolated via centrifugation

and decantation. The isolated nanoparticle material was redispersed and extracted from the centrifuge tube using ultrasonication and successive aliquots of the previously prepared XC-72/$BuNH_2$ suspension. This final mixture was then allowed to stir magnetically for 24 h in order to allow the ligand exchange and nanoparticle deposition to occur gradually. Finally, the post-deposition PtAu nanoparticle materials were isolated once more via EtOH addition and centrifugation (at 12,000 RPM for 20 min) and allowed to dry in air.

**Transmission Electron Microscopy.** Bright field TEM imaging of the samples was performed both prior to and following deposition onto the XC-72 carbon support. In preparation for analysis, each sample was dispersed in *ca.* 200 μL EtOH via sonication and drop-cast onto Formvar-coated copper TEM grids. Unsupported PtAu nanoparticle samples were imaged using a JEOL JEM-2100F transmission electron microscope operated at a 200 kV accelerating voltage. PtAu nanoparticle samples supported on XC-72 carbon powder were imaged using a Tecnai F-30 transmission electron microscope operated at a 300 kV accelerating voltage. Size distributions and mean particle diameters of the nanoparticles were measured and calculated using MacBiophotonics ImageJ software[34] using several representative images from each sample. HAADF and EDX mapping measurements were performed at the University of Birmingham (UK) using a JEOL 2100F scanning transmission electron microscope with a CEOS aberration-corrector. A JEOL annular dark field detector was used for HAADF imaging and a Bruker XFlash 4030 silicon drift detector was used for EDX mapping of the PtAu nanoparticle samples. During the EDX mapping, the HAADF-STEM images were monitored to check for possible beam-induced structure changes of the atomic structure. EDX data presented are from only those nanoparticles that did not show any visible structural changes.

**X-ray Absorption Spectroscopy.** XAS measurements were performed using the Sector 20-BM beamline of the Advanced Photon Source at Argonne National Laboratory in Argonne, IL. The end-station was equipped with a double-crystal Si(111) monochromator for wavelength selection, which was detuned to 80 % in order to help reject higher harmonics of the desired energy; a toroidal focusing mirror was also employed to further enhance harmonic rejection. Gas-ionization detectors were used to measure the absorption spectra of Pt and Au foil reference materials; however, data acquisition from the bimetallic nanoparticles was complicated by overlap between the spectra obtained at the Pt and Au $L_3$-edges (occurring at 11,562.76 eV and 11,919.70 eV, respectively[35]). This challenge was addressed by employing a 12-element Ge

fluorescence detector to collect data from the bimetallic PtAu nanoparticles. Although there also exists overlap between the Pt and Au $L_\alpha$ emission peaks centered at 9,442.3 eV and 9,713.3 eV, repectively[36]), nearly all of the interfering signal could be filtered out by excluding the overlapping energy region between the two (as depicted in Supplementary Fig. 12). While excluding this region also resulted in a reduction of fluorescence intensity, the loss was largely offset by the greater sensitivity of the fluorescence detector relative to standard absorption detectors. As a result, useable spectra were obtained for all samples through the use of this method. In order to compensate for the greater amount of noise present in the fluorescence data, PtAu nanoparticle samples were held at 90 ± 1 K during measurement in order to enhance EXAFS signal intensity by supressing thermal vibrations in the material. Full details regarding the data ranges ("k-range" and "R-range") used to obtain and fit the FT-EXAFS spectra are presented in the Supporting Information (Supplementary Table 4). Data processing and fitting were performed using WinXAS[37] and Analyzer v0.1 software, with scattering paths generated by FEFF8[38]. $S_0^2$ values for Pt and Au (both equal to 0.93) were obtained by fitting a metallic reference foil of same element. A bulk, homogeneous PtAu alloy structural model was used to calculate the Pt–M and Au–M scattering paths used in FT-EXAFS fitting. A single metal-metal scattering path was used in fitting the FT-EXAFS data because insufficient degrees of freedom were available to include separate Pt and Au scattering paths; the Pt–M and Au–M fitting values reported herein thus represent averages of the Pt–Pt/Pt–Au and Au–Au/Au–Pt contributions.

**X-ray Photoelectron Spectroscopy.** X-ray photoelectron spectroscopy (XPS) measurements were performed at Canadian Light Source in Saskatoon, Canada, using an excitation energy of 3,000 eV at the SXRMB beamline and an excitation energy of 300 eV at the SGM beamline. PtAu/C nanocatalyst samples were prepared by spreading the powder onto conductive, double-sided carbon tape, which was then affixed to a copper sample holder. Many scans of each sample were averaged together in order to obtain higher signal-to-noise ratios. Relative PtAu compositions were determined from peak areas obtained by fitting the Pt and Au 4f peaks using $Au^0/Au^+$ and $Pt^0/Pt^{2+}$ contributions in conjunction with empirically derived atomic sensitivity factors.[39] Splitting between $4f_{5/2}$ and $4f_{7/2}$ peaks was set based upon data obtained from the NIST X-ray Photoelectron Spectroscopy Database.[40] Full-width at half-maximum values for the $4f_{5/2}$ and $4f_{7/2}$ peaks within each contribution were correlated to be equal, and relative area ratios were correlated such that area($4f_{7/2}$):area($4f_{5/2}$) = 4:3. XPS valence band spectra were collected

using an excitation energy of 3,000 eV and normalized by setting the valence band maximum equal to unity.

**Cyclic Voltammetry.** Cyclic voltammetry was performed using a CHI 710 electrochemical work station with a three-electrode setup, including a polished glassy carbon working electrode (rotating disc electrode), a Ag/AgCl reference electrode, and a Pt sheet counter electrode. A solution of 0.1 M perchloric acid was used as the supporting electrolyte, with the addition of 0.1 M formic acid during FAO activity measurements. Catalyst "ink" suspensions were prepared by dispersing the carbon-supported PtAu material in EtOH via ultrasonication to obtain a final catalyst concentration of 1 $\mu g \cdot \mu L^{-1}$. A volume of the Nafion solution equal to 1 % the volume of added EtOH was then added and sonicated for a further 15 min to complete the preparation. For ORR testing, 20 μL of the catalyst ink were drop-cast onto the glassy carbon electrode surface and allowed to dry completely. A 3 μL volume of a diluted Nafion solution (20 % v/v in EtOH) was then deposited onto the dried catalyst layer in order to help improve its physical stability and electrical conductivity. The electrode surface was allowed to dry completely prior to electrochemical testing. After purging the electrolyte solution with ultrahigh purity $N_{2(g)}$, CV measurements were performed. Pt electrochemically active surface areas (ECSAs) were calculated from the integrated region beneath the H-desorption peaks in each voltammograms, whereas Au ECSAs were estimated from the integrated area of the Au–O adlayer removal peak.

**DFT Calculations.** DFT calculations were performed using Vienna *ab initio* package (VASP) software. The revised Perdew-Burke-Erzerhof (RPBE) form of the generalized-gradient approximation (GGA) was chosen for electron exchange and correlation in order to correct for the over-binding of small molecules at transition metal surfaces observed using the standard Perdew-Burke-Erzerhof approach. Although DFT-RPBE tends to overstabilize the hollow and bridge sites over the atop site for CO adsorption on Pt(111), the adsorption energies on these sites are quite close (within 0.10 eV) and in good agreement with the experimental value.[41] The electron-core interaction was described using the projector-augmented wave method (PAW). A kinetic energy cutoff of 450 eV was used for the planewaves, and the Brillouin zone was sampled using a 3×3×1 Monkhorst-Pack scheme. The surface model slab was created using a 4×4 supercell of the Pt/Au unit cell, with four atomic layers and a 15 Å unit cell. Adsorption energies were calculated using the following equation:

$$E_{ads} = E_{surface+adsorbate} - (E_{surface} + E_{adsorbate})$$

wherein the energy of the adsorbate, $E_{adsorbate}$, was computed by placing the CO adsorbate molecule in a 10 Å wide cubic cell vacuum to prevent intermolecular interactions resulting from the periodic boundary conditions.

**Data availability.**

The data supporting the results of this work are available from the authors on reasonable requests.